



# Potassium hydride-intercalated graphite as an efficient heterogeneous catalyst for ammonia synthesis

Fei Chang<sup>1</sup>, Ilker Tezsevin<sup>2</sup>, Jan Willem de Rijk<sup>1</sup>, Johannes D. Meeldijk<sup>1,3</sup>, Jan P. Hofmann<sup>4,5</sup>, Süleyman Er<sup>2</sup>, Peter Ngene<sup>1</sup>✉ and Petra E. de Jongh<sup>1</sup>✉

**Due to the high energy needed to break the  $\text{N}\equiv\text{N}$  bond ( $945\text{ kJ mol}^{-1}$ ), a key step in ammonia production is the activation of dinitrogen, which in industry requires the use of transition metal catalysts such as iron (Fe) or ruthenium (Ru), in combination with high temperatures and pressures. Here we demonstrate a transition-metal-free catalyst—potassium hydride-intercalated graphite ( $\text{KH}_{0.19}\text{C}_{24}$ )—that can activate dinitrogen at very moderate temperatures and pressures. The catalyst catalyses  $\text{NH}_3$  synthesis at atmospheric pressure and achieves  $\text{NH}_3$  productivity ( $\mu\text{mol}_{\text{NH}_3}\text{ g}_{\text{cat}}^{-1}\text{ h}^{-1}$ ) comparable to the classical noble metal catalyst Ru/MgO at temperatures of 250–400 °C and 1 MPa. Both experimental and computational calculation results demonstrate that nanoconfinement of potassium hydride between the graphene layers is crucial for the activation and conversion of dinitrogen. Hydride in the catalyst participates in the hydrogenation step to form  $\text{NH}_3$ . This work shows the promise of light metal hydride materials in the catalysis of ammonia synthesis.**

Ammonia is a key feedstock in the production of fertilizers and is regarded as a promising hydrogen carrier for future renewable energy infrastructure<sup>1,2</sup>. The conversion of  $\text{N}_2$  and  $\text{H}_2$  to  $\text{NH}_3$  is exergonic and thermodynamically favourable at ambient conditions. However, owing to the strong triple covalent bond in the  $\text{N}_2$  molecule and high kinetic barriers, ammonia synthesis is usually conducted at high temperatures and pressures (400–500 °C, 10–30 MPa) using either fused iron catalysts (Haber–Bosch process) or alkali-promoted ruthenium (Ru) catalysts (Kellogg advanced ammonia process)<sup>3–5</sup>. The entire ammonia synthesis process (including the energy used to produce  $\text{H}_2$ ) is highly energy intensive (consuming >1% of the annual global energy supply) and affordable only in large-scale facilities<sup>6</sup>. Therefore, it is attractive to explore catalysts that would work under milder temperatures and pressures.

The rate-determining step for traditional ammonia synthesis is the breaking of the stable  $\text{N}\equiv\text{N}$  bond ( $945\text{ kJ mol}^{-1}$ ) and/or the subsequent removal of ammonia from the catalyst surface<sup>7</sup>. Recent research has focused on the creation of catalytically active centres that readily cleave  $\text{N}_2$  molecules and, concomitantly, bind  $\text{NH}_x$  species only weakly<sup>8</sup>. Common strategies include modification of the electronic states of transition metal active centres with electron donors and/or the use of new support materials<sup>9</sup>. For instance, systematic studies show that the use of electride-based supports, which typically have low work functions (2.3–3.5 eV) and strong electron donation ability, can significantly decrease activation barriers and promote ammonia synthesis using Ru or Co catalysts<sup>10,11</sup>. The use of pre-reduced rare earth oxide supports (for example,  $\text{La}_{0.5}\text{Ce}_{0.5}\text{O}_{1.75}$ ) was recently reported to weaken the  $\text{N}\equiv\text{N}$  bond on Ru nanoparticles and greatly enhance catalytic activity via strong metal–support

interaction<sup>12</sup>.  $\text{SrZrO}_3$  supports increased the ammonia production rate of Ru catalysts due to facile nitrogen activation with the formation of a  $\text{N}_2\text{H}$  intermediate<sup>13</sup>.

A recent development in catalytic ammonia synthesis is the use of metal hydride- and oxyhydride-based materials as catalysts or promoters<sup>9</sup>. With the addition of alkali (earth) metal hydrides such as LiH, NaH, KH and  $\text{BaH}_2$ , transition metals (Mn, Fe, Co and so on) exhibit, by two to four orders of magnitude, higher ammonia synthesis activities, lower apparent activation energies (apparent activation energy ( $E_a$ ) = 40–60  $\text{kJ mol}^{-1}$ ) and an unusual catalytic mechanism (metal hydride as the second catalytic centre abstracting nitrogen species from transition metals)<sup>14–16</sup>. Likewise, continuous ammonia formation was observed on hydride-containing Ti compounds ( $\text{TiH}_2$  and  $\text{BaTiO}_{2.5}\text{H}_{0.5}$ ) even without Ru or Fe<sup>17,18</sup>. Azofra et al. reported a silica-grafted, Mo-hydride, single-site catalyst able to catalyse ammonia production at a rate of  $1.3\text{ mmol g}_{\text{Mo}}^{-1}\text{ h}^{-1}$  at approximately 400 °C<sup>19</sup>. In another study, Kitano et al. showed that a self-assembled Ru– $\text{Ba}(\text{NH}_2)_2$  core-shell structure enhanced the turnover frequency of Ru by two orders of magnitude at <300 °C<sup>10</sup>. The impressive performance of transition metal catalysts supported on metal (oxy)hydrides is attributed to the presence of (oxy)hydrides that promote  $\text{N}_2$  dissociation on transition metals by enhancing the electron transfer process from the bonding orbitals of the transition metals to the antibonding- $\pi$  orbitals of  $\text{N}_2$  molecules. Although these findings clearly demonstrate the importance of metal hydrides, oxyhydrides and electrides in mediation of ammonia synthesis, transition metals are still used as indispensable catalytic centres in all these catalysts.

Nanoconfinement of metal hydrides in porous hosts often leads to intriguing properties related to reversible hydrogen storage, ionic

<sup>1</sup>Materials Chemistry and Catalysis, Debye Institute for Nanomaterials Science, Utrecht University, Utrecht, the Netherlands. <sup>2</sup>Dutch Institute for Fundamental Energy Research, Eindhoven, the Netherlands. <sup>3</sup>Electron Microscopy Center, Utrecht University, Utrecht, the Netherlands. <sup>4</sup>Laboratory for Inorganic Materials and Catalysis, Department of Chemical Engineering and Chemistry, Eindhoven University of Technology, Eindhoven, the Netherlands. <sup>5</sup>Present address: Surface Science Laboratory, Department of Materials and Earth Sciences, Technical University of Darmstadt, Darmstadt, Germany.

✉e-mail: P.Ngene@uu.nl; P.E.dejongh@uu.nl

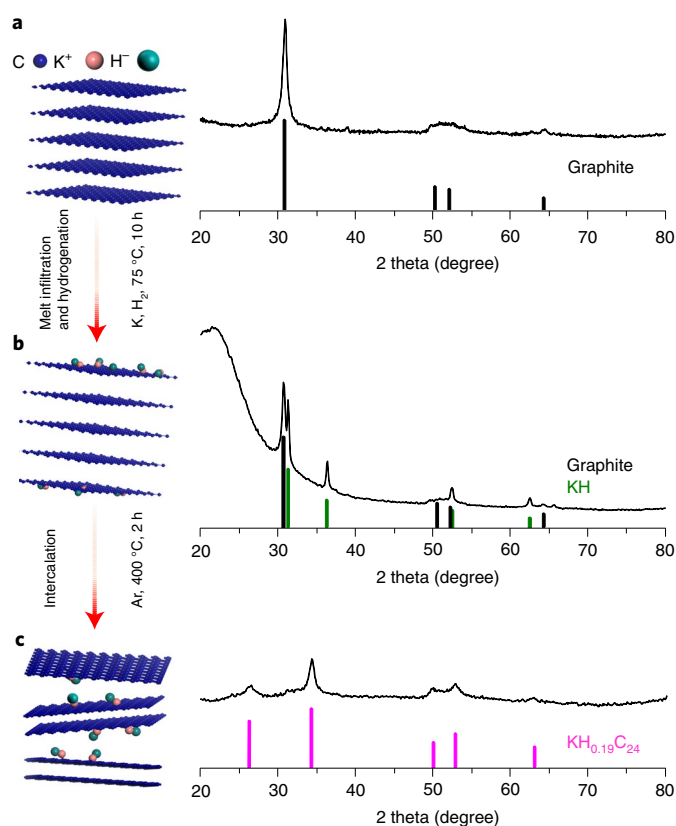


**Fig. 1 | Schematic illustration of the preparation process of the  $\text{KH}_{0.19}\text{C}_{24}$  catalyst and XRD patterns.** **a**, Graphite nanoplatelets (GNP500) were used as the carbon host. Right: XRD pattern of GNP500. **b**, The graphite-supported KH sample was prepared by melt infiltration and hydrogenation. Right: XRD pattern of 15 wt% KH on graphite. Diffraction peaks of KH (ICDD-PDF-01-089-2778) and graphite (ICDD-PDF-00-001-0640) were observed. KH crystallites had an average size of 11 nm (calculated using the Scherrer equation). **c**, The  $\text{KH}_{0.19}\text{C}_{24}$  catalyst was prepared by heating the KH-graphite sample in Ar to 400 °C for 2 h. Right: XRD pattern of the prepared  $\text{KH}_{0.19}\text{C}_{24}$  catalyst. Diffraction peaks correspond to those of the potassium hydride-graphite intercalation compound  $\text{KH}_{0.19}\text{C}_{24}$  (ICDD-PDF-00-024-0852).

conduction and catalysis<sup>20–22</sup>. In this work, we show that nanoconfinement of potassium hydride in turbostratic carbon materials leads to intercalation (insertion) of potassium and hydride ions between the graphene layers. The newly formed nanocomposites are able to activate dinitrogen and act as an efficient and stable transition-metal-free catalyst for ammonia synthesis under conditions of 250–400 °C and 0.1–1.0 MPa. Hydride in the lattice of the  $\text{KH}_{0.19}\text{C}_{24}$  catalyst plays an important role in  $\text{N}_2$  activation and is involved in the hydrogenation step to form  $\text{NH}_3$ . Our experimental and density-functional theory (DFT) calculation results suggest that ammonia synthesis over potassium hydride-intercalated graphite tends to follow an alternating associative mechanism.

## Results

**Catalyst synthesis and characterization.** In graphite intercalation compounds (GICs), guest species are usually intercalated in the galleries between graphene layers of the carbon matrix<sup>21</sup>. Depending on the type of intercalant, the synthesis methods used for GICs differ. In general, there are two ways to prepare alkali metal hydride-graphite intercalation compounds: one is the direct intercalation of alkali metal hydride via solid–solid or liquid–solid interaction/reaction between host and guest; the second is the chemisorption

and reaction of dihydrogen with alkali metal–graphite intercalation precursors<sup>23</sup>. In this study, graphite nanoplatelets (a type of carbon material consisting of stacks of graphene layers with a thickness of a few nanometres) were employed as the host. Graphite nanoplatelets have a high specific surface area ( $500\text{ m}^2\text{ g}^{-1}$ ) and porosity due to the interplatelet space. The potassium hydride-intercalated graphite catalyst was prepared by deposition of KH on the graphitic carbon (via infiltration of molten potassium and hydrogenation to KH) followed by partial decomposition of the potassium hydride, which led to intercalation of KH into the graphene layers. Figure 1 shows the synthesis protocol. The carbon host shows typical diffraction peaks for graphite (Fig. 1a). The diffraction peaks of KH can be clearly observed (Fig. 1b) after melt infiltration and hydrogenation, suggesting that KH crystallites with an average size of 11 nm were formed on the surface of the graphite. Subsequently, this KH-graphite sample was heated to 400 °C for 2 h in Ar. Partial dehydrogenation of KH (Supplementary Fig. 1) during the heating process probably facilitates the intercalation of KH and formation of potassium hydride-intercalated graphite  $\text{KH}_{0.19}\text{C}_{24}$  (see X-ray diffraction (XRD) pattern in Fig. 1c; its crystallographic parameters are shown in Supplementary Table 1). The absence of KH diffraction peaks indicates that KH was highly dispersed. Nitrogen physisorption (Supplementary Fig. 2 and Supplementary Table 2) demonstrates that the prepared  $\text{KH}_{0.19}\text{C}_{24}$  catalyst maintained the porous structure of the graphitic carbon, but that the surface area was reduced ( $192\text{ m}^2\text{ g}^{-1}$ ). This shows that the intercalation of K and H, concomitant with release of  $\text{H}_2$ , modified the texture/structure and crystallinity of the graphitic carbon.

**Evaluation of ammonia synthesis activity.** The obtained  $\text{KH}_{0.19}\text{C}_{24}$  material, stored in a glovebox, was placed in an airtight fixed-bed reactor for the study of ammonia synthesis performance. A mixture of  $\text{H}_2$  and  $\text{N}_2$  (molar ratio of 3:1) was used as reactant. The reactor outlet was bubbled through a sulfuric acid solution connected to a conductivity meter for quantitative monitoring of  $\text{NH}_3$  production (Supplementary Figs. 3 and 4). In addition, we also used mass spectrometry to double-check the nature of the products (Supplementary Fig. 5). It is clear that the product formed was ammonia, and productivity was similar to that derived from conductivity tests. Figure 2a shows continuous  $\text{NH}_3$  production over the  $\text{KH}_{0.19}\text{C}_{24}$  catalyst at different temperature stages (250–400 °C) under a pressure of 1 MPa and a space velocity of  $2,000\text{ ml g}_{\text{cat}}^{-1}\text{ h}^{-1}$  over 65 h. Catalytic activity started at 250 °C. Both the yield of  $\text{NH}_3$  and the conversion of  $\text{N}_2$  increased with temperature (Fig. 2a and Supplementary Fig. 6). An  $\text{NH}_3$  concentration of 8,900 ppm (corresponding to  $\text{N}_2$  conversion of 1.7%) was achieved at 400 °C. This activity remained constant over 20 h, which reveals the high activity and stability of the  $\text{KH}_{0.19}\text{C}_{24}$  catalyst. As a control experiment, ammonia synthesis activity in a blank reactor (without a catalyst) was quite negligible (Supplementary Fig. 7). The accumulated turnover number on the  $\text{KH}_{0.19}\text{C}_{24}$  catalyst was about 34 over the 65-h test period (Supplementary Fig. 8), which indicates that ammonia was produced catalytically rather than by any stoichiometric reaction. We also tested ammonia synthesis performance on the  $\text{KH}_{0.19}\text{C}_{24}$  catalyst under a pure  $\text{N}_2$  flow (Supplementary Fig. 9). However, no significant  $\text{NH}_3$  production rate was observed, suggesting that the presence of dihydrogen in the gas phase is essential for the conversion of  $\text{N}_2$  to  $\text{NH}_3$ .

Because Ru is the element most active for ammonia synthesis, we compared the catalytic activity of  $\text{KH}_{0.19}\text{C}_{24}$  with the reference 5 wt% Ru/MgO catalyst (Fig. 2b). To achieve higher  $\text{NH}_3$  production rates, a higher space velocity ( $36,000\text{ ml g}_{\text{cat}}^{-1}\text{ h}^{-1}$ ) was used for these measurements. In our study, the  $\text{KH}_{0.19}\text{C}_{24}$  catalyst exhibited  $\text{NH}_3$  production rates of 502, 999 and  $1,641\text{ }\mu\text{mol g}_{\text{cat}}^{-1}\text{ h}^{-1}$  at 300, 325 and 350 °C, respectively, which are between one and ten times higher than the corresponding rates for 5 wt% Ru/MgO. The

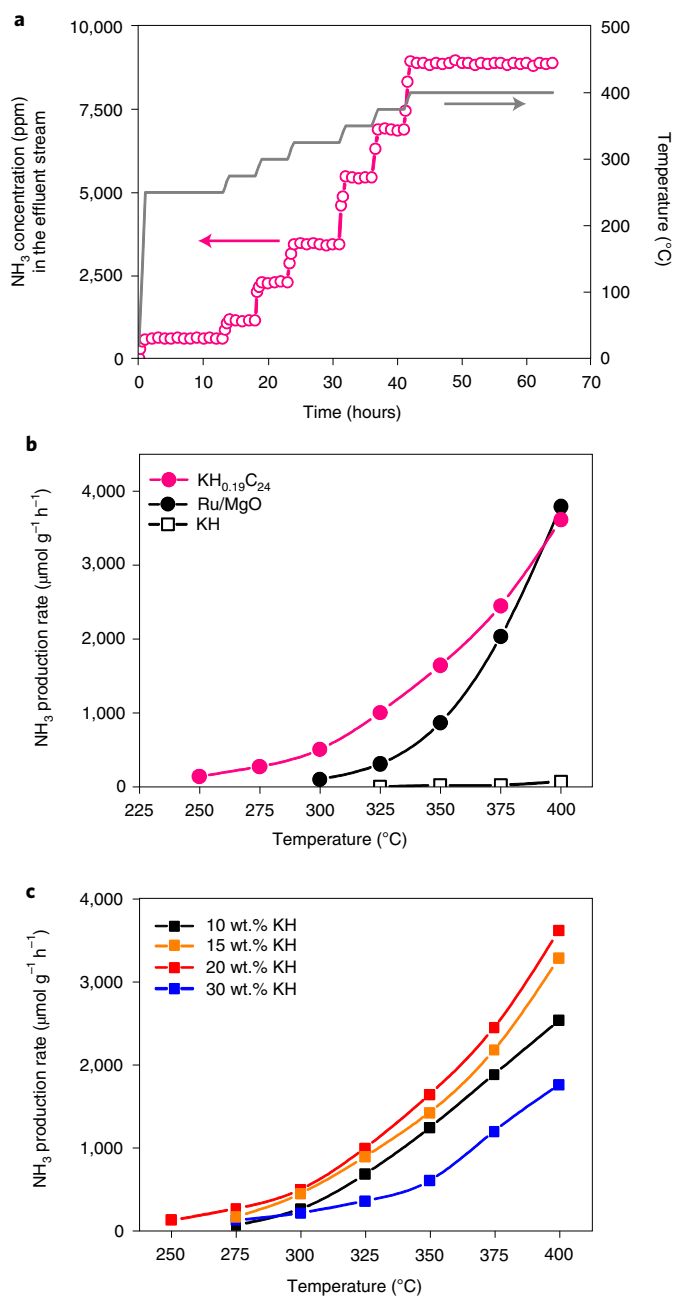


**Fig. 2 | NH<sub>3</sub> synthesis catalysed by KH<sub>0.19</sub>C<sub>24</sub>.** **a**, Time on stream for NH<sub>3</sub> production on the KH<sub>0.19</sub>C<sub>24</sub> catalyst under a gas flow of N<sub>2</sub> and H<sub>2</sub> (molar ratio 1:3). Reaction conditions: 1 MPa, 250–400 °C and SV = 2,000 ml g<sub>cat</sub><sup>-1</sup> h<sup>-1</sup>. The yield of NH<sub>3</sub> (in ppm) increased with reaction temperature. KH<sub>0.19</sub>C<sub>24</sub> was stable during the 65-h test. **b**, Temperature dependence of NH<sub>3</sub> production rate of KH<sub>0.19</sub>C<sub>24</sub> and of 5 wt% Ru/MgO and KH. Reaction conditions: 1 MPa, 250–400 °C and SV = 36,000 ml g<sub>cat</sub><sup>-1</sup> h<sup>-1</sup>. **c**, Temperature dependence of NH<sub>3</sub> production rate of KH<sub>0.19</sub>C<sub>24</sub> prepared with different KH loadings. Reaction conditions: 1 MPa, 250–400 °C and SV = 36,000 ml g<sub>cat</sub><sup>-1</sup> h<sup>-1</sup>.

KH<sub>0.19</sub>C<sub>24</sub> catalyst even produced 792 μmol NH<sub>3</sub> g<sub>cat</sub><sup>-1</sup> h<sup>-1</sup> at ambient pressure (Supplementary Fig. 10), proving its promising performance also under mild conditions. On the other hand, turnover frequency (TOF) of ammonia synthesis on KH<sub>0.19</sub>C<sub>24</sub> was lower than that of 5 wt% Ru/MgO (Supplementary Table 3). It is worth noting that because K species are intercalated and not available as metallic surfaces, it is not possible to measure K dispersion via traditional

chemisorption or titration methods. Here we consider all K atoms as active sites, which gives a lower limit of the real TOF of our catalyst. Because KH itself is inactive under the applied reaction conditions, intercalation of KH between the graphene layers is crucial for catalytic activity. In addition, the effect of nanoconfinement on the concentration of hydride vacancies, which are essential for the dissociation of H<sub>2</sub>, explains why KH<sub>0.19</sub>C<sub>24</sub> shows promising activity but not KH.

The performance of KH<sub>0.19</sub>C<sub>24</sub> catalysts with different KH loadings in precursor (10–30 wt%) is shown in Fig. 2c. The catalyst prepared with 20 wt% KH loading showed the highest NH<sub>3</sub> production rate at 250–400 °C. If we assume that all potassium in this KH<sub>0.19</sub>C<sub>24</sub> catalyst (20 wt% loading) acts as an active site, turnover frequencies of the KH<sub>0.19</sub>C<sub>24</sub> catalyst at different temperatures can be calculated (Supplementary Fig. 11). KH<sub>0.19</sub>C<sub>24</sub> showed turnover frequencies of 0.28 × 10<sup>-4</sup>, 0.91 × 10<sup>-4</sup> and 2.1 × 10<sup>-4</sup> s<sup>-1</sup> at 300, 350 and 400 °C, respectively, which were 9.1, 6.5 and 3.3 times higher than those for a recently reported Mn<sub>4</sub>N-KH composite catalyst<sup>15</sup>. We also investigated the effect of the nature of carbon material on the formation of KH<sub>0.19</sub>C<sub>24</sub> and ammonia synthesis activity (Supplementary Figs. 12 and 13). The use of amorphous carbon (carbon aerogel) or carbon nanofibres did not lead to the formation of KH<sub>0.19</sub>C<sub>24</sub> and gave very low ammonia production rates. Graphitic carbon materials, such as non-porous graphite (NPG), can be intercalated by KH but yield an NH<sub>3</sub> production rate of only 154 μmol g<sub>cat</sub><sup>-1</sup> h<sup>-1</sup> at 400 °C. This can be explained by the low surface area and pore volume and large KH<sub>0.19</sub>C<sub>24</sub> crystallites (>40 nm), which create fewer active sites. Employing other graphitic high-surface-area carbon materials (GNP750 or HSAG500) as host indeed led to the formation of KH<sub>0.19</sub>C<sub>24</sub> and showed an activity of 2,800 μmol g<sub>cat</sub><sup>-1</sup> h<sup>-1</sup> at 400 °C and 1 MPa. Hence a high surface area and crystallinity of the carbon host are essential for the formation of active catalysts.

Elemental analysis (inductively coupled plasma-optical emission spectrometry, ICP-OES) (Supplementary Table 4) and energy-dispersive X-ray spectroscopy (EDX) analysis of the KH<sub>0.19</sub>C<sub>24</sub> catalyst (Fig. 3c) showed that the concentration of transition metal impurities (which are sometimes found in carbon materials) was below the detection limit (<0.01%). Furthermore, we prepared 0.2 wt% Fe- or 0.2 wt% Ni-doped KH<sub>0.19</sub>C<sub>24</sub> samples and investigated the influence of the presence of these low amounts of transition metals on the NH<sub>3</sub> synthesis performance of the KH<sub>0.19</sub>C<sub>24</sub> catalyst. These transition-metal-doped catalysts exhibited similar or slightly lower activities compared to the pure KH<sub>0.19</sub>C<sub>24</sub> catalyst (Supplementary Fig. 14), which excludes promotion by transition metal contamination as an explanation for the high activity of KH<sub>0.19</sub>C<sub>24</sub> catalysts.

**Catalyst characterization after tests.** We used a variety of techniques to characterize the KH<sub>0.19</sub>C<sub>24</sub> catalyst after NH<sub>3</sub> synthesis. XRD shows the same phase in the diffractogram for the KH<sub>0.19</sub>C<sub>24</sub> catalyst following catalysis (Supplementary Fig. 15), but the diffraction peaks are slightly broader than those of the fresh catalyst, suggesting a slight change in the structure or composition. This indicates that the final structure of the catalyst is probably formed following exposure to the reaction mixture. Although nitrogen physisorption indicated that the porous structure was preserved (Supplementary Fig. 16), the surface area of the KH<sub>0.19</sub>C<sub>24</sub> catalyst decreased to 106 m<sup>2</sup> g<sup>-1</sup>. Elemental analysis results (Supplementary Table 4) show that the potassium content in the KH<sub>0.19</sub>C<sub>24</sub> catalyst after operation at 250–400 °C for 65 h was 11.14 wt%, which is quite close to the 11.89 wt% obtained for the fresh catalyst. This proves the stability of the catalyst. The minute amount of K removed during the reaction could be explained by decomposition of non-intercalated KH in the freshly prepared sample, leading to evaporation of K. The local structure and surface composition of the KH<sub>0.19</sub>C<sub>24</sub> catalyst after catalytic testing were evaluated using high-angle annular dark

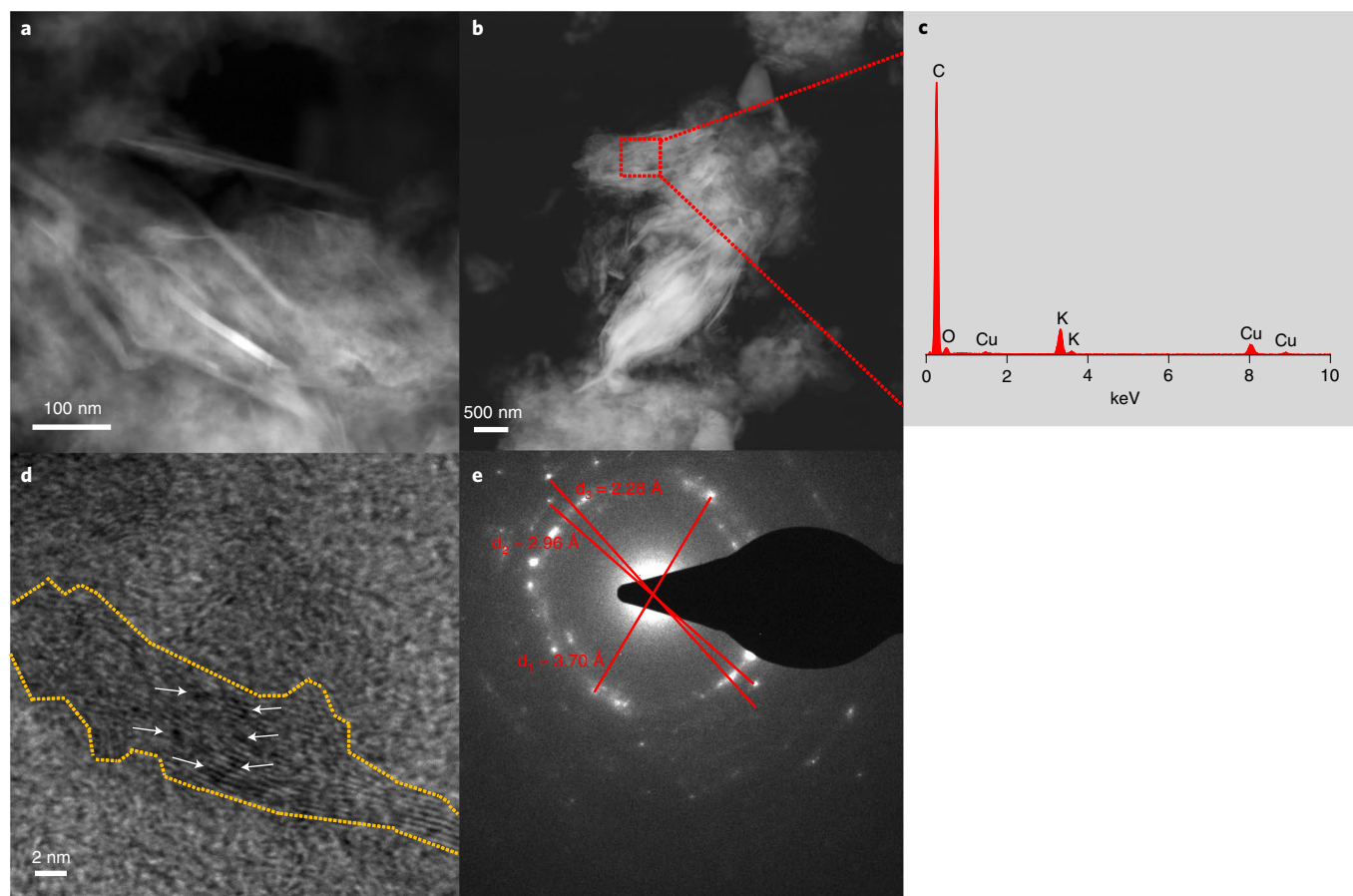


**Fig. 3 | Electron microscopy analyses of the  $\text{KH}_{0.19}\text{C}_{24}$  catalyst after ammonia synthesis.** **a,b**, HAADF-STEM images of the  $\text{KH}_{0.19}\text{C}_{24}$  catalyst after ammonia synthesis with scale bars of 100 nm (**a**) and 500 nm (**b**). **c**, EDX analysis of the selected area. Oxygen was detected, indicating the presence of oxygen-containing functional groups on the carbon host. The Cu signal is from the sample grid. No other impurities were detected. **d**, HR-TEM image of the  $\text{KH}_{0.19}\text{C}_{24}$  catalyst after ammonia synthesis. White arrows indicate elongated material filling in between the graphene layers, attributed to intercalated KH. **e**, Electron diffraction pattern of the  $\text{KH}_{0.19}\text{C}_{24}$  catalyst after ammonia synthesis. The planar distances of  $\text{KH}_{0.19}\text{C}_{24}$  were calculated, which matched well with the results obtained from the XRD pattern (Supplementary Fig. 15).

field-scanning transmission electron microscopy (HAADF-STEM) and EDX. Electron micrographs (Fig. 3a,b) showed a layered structure for the  $\text{KH}_{0.19}\text{C}_{24}$  catalyst, attributed to the stacks of graphene layers. No KH crystallites/domains were observed in or on the carbon matrix, suggesting that KH was highly dispersed. EDX analysis in the selected region (Fig. 3c) revealed that K was indeed present in the sample. High-resolution-transmission electron microscopy (HR-TEM) imaging (Fig. 3d) shows lattice fringes of graphite, a widened distance between the carbon layers and elongated material between these layers, which is probably intercalated KH (denoted by white arrows). Electron diffraction (Fig. 3e) gave planar distances of 3.70, 2.96 and 2.28 Å for graphene layers in the  $\text{KH}_{0.19}\text{C}_{24}$  catalyst, which are consistent with the results obtained from XRD (Supplementary Fig. 15).

**Mechanistic investigations.** Ammonia synthesis on heterogeneous catalysts involves the adsorption/activation of  $\text{N}_2$  and  $\text{H}_2$  and hydrogenation of nitrogen species/intermediates to form  $\text{N}_x\text{H}_y$  and eventually  $\text{NH}_3$  on the catalyst surface. Previous studies reported that alkali metal hydrides are converted to amides or imides during ammonia synthesis<sup>10,14,15</sup>. In this section, we discuss the  $\text{N}_2$  activation and hydrogenation processes over the  $\text{KH}_{0.19}\text{C}_{24}$  catalysts as well as potential nitrogen adsorption intermediates. A fresh  $\text{KH}_{0.19}\text{C}_{24}$  catalyst was treated with 0.5 MPa  $\text{N}_2$  at 300 °C for 20 h. X-ray photoelectron spectroscopy (XPS) was used to probe

the catalyst surface before and after  $\text{N}_2$  treatment. The potassium 2*p* and carbon 1*s* spectra of the fresh  $\text{KH}_x\text{C}_{24}$  catalyst are shown in Supplementary Fig. 17. In the C 1*s* region, besides graphitic carbon (284.5 eV), surface functional groups (COOH, C-OH and C=O) of graphite were detected. The K 2*p* spectrum has two spin-orbit split peaks at  $\text{BE}(\text{K}2p_{3/2}) = 293.2$  eV and  $\text{BE}(\text{K}2p_{1/2}) = 295.9$  eV, which we attribute to positively charged K. After treatment in  $\text{N}_2$ , no phase change or shift in binding energies of K 2*p* or C 1*s* was observed (Fig. 4a,b). However, a broad N 1*s* peak at  $\text{BE}(\text{N}1s) = 399.2$  eV was observed (Fig. 4c), which confirms that dinitrogen can be activated on the surface of the  $\text{KH}_{0.19}\text{C}_{24}$  catalyst. This N 1*s* spectrum is significantly different from that of  $\text{KNH}_2$  (Supplementary Fig. 18). Ertl and Thiele identified the N 1*s* peak at ~400 eV on Fe as adsorbed  $\text{N}_2$  or  $\text{NH}_3$  species<sup>24</sup>. However, because the N 1*s* signal is weak, it is hard to unequivocally determine the nature of nitrogen species on  $\text{KH}_{0.19}\text{C}_{24}$ . In addition, Ar-temperature-programmed desorption (Ar-TPD) of the  $\text{N}_2$ -treated sample (Supplementary Fig. 19) showed only the release of  $\text{N}_2$ , which indicates that adsorbed nitrogen species are very probably predominantly in the form of dinitrogen (or reversibly form dinitrogen on heating). Therefore, the direct dissociation of  $\text{N}_2$  on  $\text{KH}_{0.19}\text{C}_{24}$  is not plausible.

To investigate the hydrogenation step, the  $\text{N}_2$ -treated  $\text{KH}_{0.19}\text{C}_{24}$  sample was heated in a flow of 5%  $\text{H}_2/\text{Ar}$  and the outlet gas monitored by mass spectrometry. As shown in Fig. 4d, a considerable amount of  $\text{NH}_3$  ( $m/z = 17$ ) was released between 100 and 300 °C.

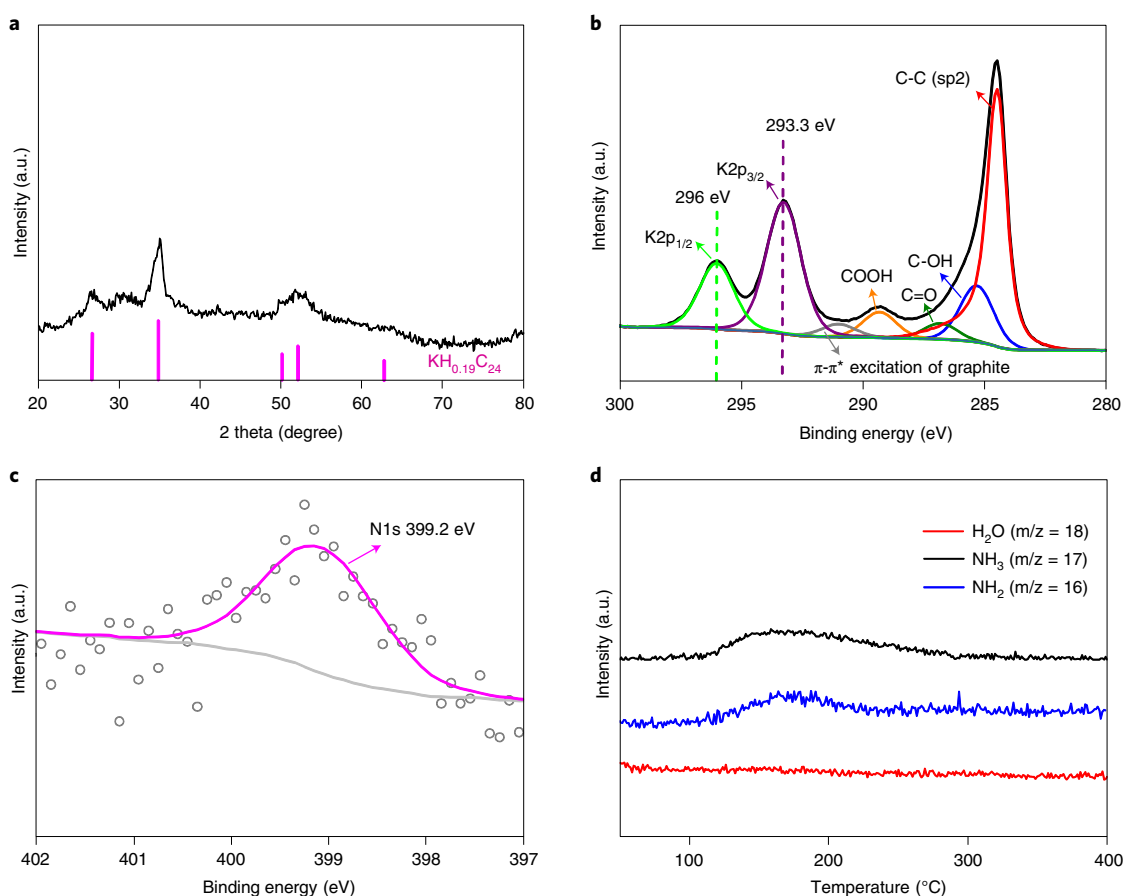


**Fig. 4 | Characterization of the  $N_2$ -treated  $KH_{0.19}C_{24}$  catalyst.** **a**, XRD pattern of the  $KH_{0.19}C_{24}$  catalyst after treatment in  $N_2$ , showing  $KH_{0.19}C_{24}$  as the main crystalline phase following  $N_2$  activation. **b,c**, XPS of the  $KH_{0.19}C_{24}$  catalyst after treatment with  $N_2$ , **b**, K 2p and C 1s spectra. The binding energies of the K 2p doublet were 296.0 and 293.3 eV, corresponding to positively charged K. **c**, N 1s spectrum. A broad N 1s peak at 399.2 eV was observed, indicating nitrogen-containing surface species after treatment with  $N_2$ . **d**, Temperature-programmed reaction over the  $N_2$ -treated  $KH_{0.19}C_{24}$  sample in a flow of 5%  $H_2/Ar$  ( $H_2$ -TPR). Sample weight was 30 mg and ramp rate  $5^\circ C\ min^{-1}$ . The  $NH_3$  signal ( $m/z=17$ ),  $NH_2$  signal ( $m/z=16$ ) and  $H_2O$  signal ( $m/z=18$ ) were monitored by mass spectrometry. The broad  $NH_3$  signal produced at 100–300  $^\circ C$  originated from the hydrogenation of surface nitrogen species.

This  $NH_3$  probably originated from hydrogenation of the surface nitrogen species. Remarkably, the initial temperature (100  $^\circ C$ ) of ammonia production is comparable to that of the recently reported state-of-the-art catalyst based on the chemical looping process<sup>25</sup>. As a control experiment, a potassium carbide sample ( $KC_{24}$ ) was treated with  $N_2$  and  $H_2$  successively in the same manner. Neither was N detected with XPS (Supplementary Fig. 20) nor was  $NH_3$  produced using  $H_2$ -temperature-programmed reaction (TPR) (Supplementary Fig. 21). These results indicate the critical role of hydride ions in the promotion of  $N_2$  activation and hydrogenation.

We conducted H/D isotopic experiments to gain further insight into the role of potassium hydride in hydrogen dissociation and ammonia production. The  $D_2$ -TPR profile of the  $KH_{0.19}C_{24}$  catalyst shows the evolution of HD following heating (Supplementary Fig. 22), demonstrating the facile exchange of lattice hydride with  $D_2$  in the gas phase and hence evidence that hydrogen dissociation/activation occurs on the  $KH_{0.19}C_{24}$  catalyst under mild conditions. Supplementary Fig. 23 presents the evolution of ammonia on a  $N_2$ -pretreated  $KH_{0.19}C_{24}$  catalyst when switching the gas flow from Ar to  $D_2/Ar$  at 300  $^\circ C$ . On switching the atmosphere,  $NH_3$  and its isotope products ( $NDH_2$ ,  $ND_2H$  and  $ND_3$ ) were detected. Interestingly, only  $NH_3$  was detected initially, as well as mixed products, whereas the signals of both mixed isotopic products and  $ND_3$

later became dominant. Therefore, the lattice hydride in  $KH_{0.19}C_{24}$  is involved in catalytic hydrogenation as a hydrogen source.

Kinetic analysis was conducted to deduce the  $E_a$  and reaction orders with respect to  $N_2$ ,  $H_2$  and  $NH_3$  (Fig. 5).  $E_a$  of the  $KH_{0.19}C_{24}$  catalyst obtained over a reaction temperature range of 250–350  $^\circ C$  was only 62.3  $kJ\ mol^{-1}$ , which is much lower than that for Ru-based catalysts. For example, the  $E_a$  of Ru/MgO is 117  $kJ\ mol^{-1}$  (Supplementary Fig. 24) and for Cs-promoted Ru/MgO it is 109–124  $kJ\ mol^{-1}$  (ref. 26). This demonstrates the low kinetic barriers for ammonia synthesis over  $KH_{0.19}C_{24}$ . Conventional Ru catalysts usually adsorb hydrogen strongly, leading to blocking of the active sites for  $N_2$  adsorption and thus displaying a negative reaction order in  $H_2$  ( $\gamma = -0.5$  to  $\sim -1.2$ )<sup>27</sup>. The reaction order in  $H_2$  over  $KH_{0.19}C_{24}$  is close to zero ( $\gamma = 0.2$ ), meaning that blocking of the active sites by adsorbed hydrogen does not play an important role in the case of  $KH_{0.19}C_{24}$ . The reaction order in  $N_2$  over the  $KH_{0.19}C_{24}$  catalyst is close to unity ( $\beta = 0.81$ ), suggesting that coverage with  $N_2$  is relatively low and that the activation/dissociation of  $N_2$  over  $KH_{0.19}C_{24}$  is a slow step<sup>7,18</sup>. Furthermore the reaction order in  $NH_3$  is  $-1.5$  over  $KH_{0.19}C_{24}$ . This value is similar to that of the industrial Fe catalyst KM1 (ref. 28), implying that  $NH_3$  populates and binds strongly on the catalyst surface.

In addition we performed DFT calculations to evaluate the most likely  $N_2$  adsorption sites, as well as different ammonia synthesis

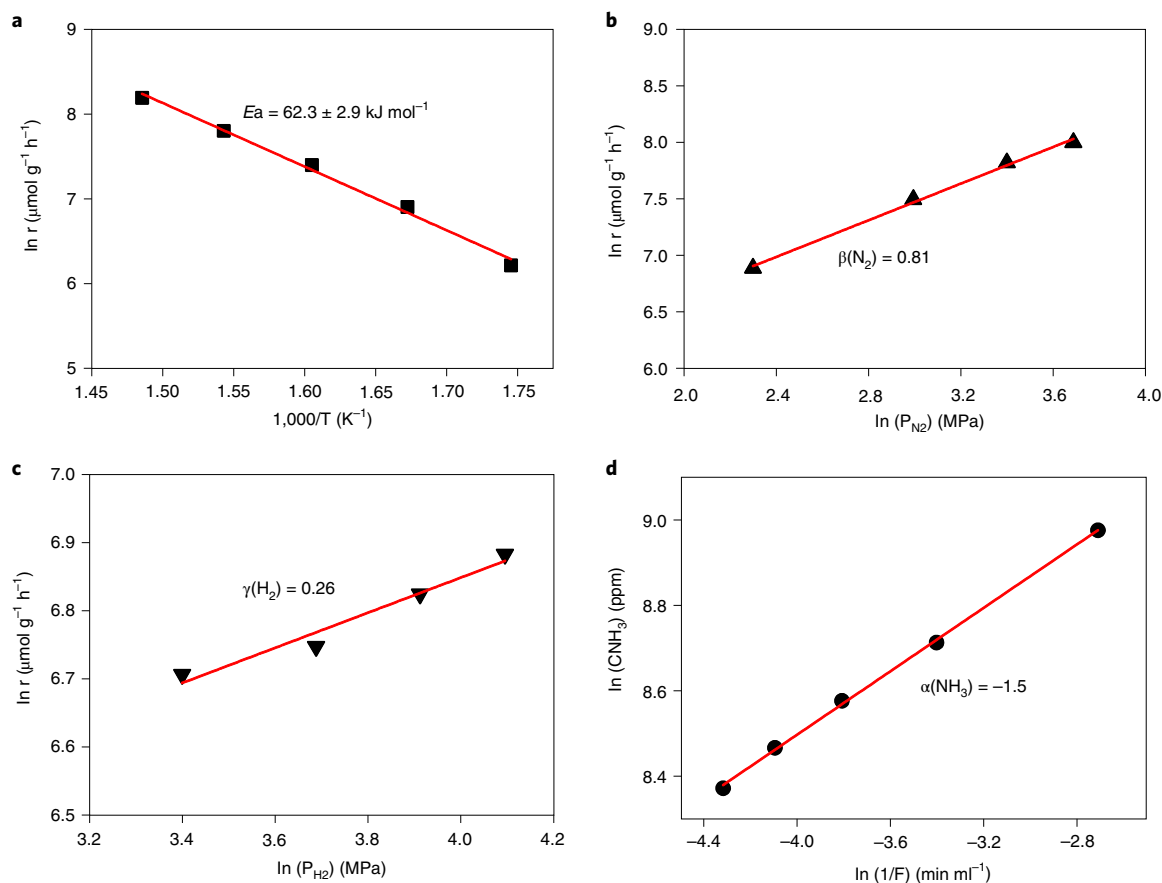


**Fig. 5 | Kinetic analyses of ammonia synthesis on the  $\text{KH}_{0.19}\text{C}_{24}$  catalyst.** **a**, Arrhenius plot and  $E_a$  for the  $\text{KH}_{0.19}\text{C}_{24}$  catalyst. Reaction conditions: 1 MPa, 250–400 °C and  $\text{SV} = 36,000 \text{ ml g}_{\text{cat}}^{-1} \text{h}^{-1}$ . The error in activation energies reflects the error of linear fit of Arrhenius plots. **b–d**, Reaction orders of the  $\text{KH}_{0.19}\text{C}_{24}$  catalyst with respect to  $\text{N}_2$  (**b**),  $\text{H}_2$ , (**c**) and  $\text{NH}_3$  (**d**).

pathways on KH-intercalated graphite, represented by a supercell model corresponding to  $\text{K}_4\text{HC}_{96}$  (Supplementary Fig. 25). In this optimized structure the intercalation interlayer spacing was  $3.92 \text{ \AA}$ , which matches with the experimental value of  $4.03 \text{ \AA}$  and thus proves the model's reliability. Bader charge analyses on this DFT-optimized structure show that the average charge of K and H atoms in the intercalated  $\text{K}_4\text{H}$  active centre was  $+0.79$  and  $-0.80$ , respectively, which are also close to their chemical states in potassium hydride.

We first investigated the feasibility of activation/dissociation of  $\text{N}_2$  and  $\text{H}_2$  in simulation cells, respectively. The adsorption energies of the  $\text{N}_2$  molecule on the graphite surface, between the graphene layers and on the  $\text{K}_4\text{H}$  cluster intercalated between the two graphene layers, were  $-0.13$ ,  $0.62$  and  $-0.85 \text{ eV}$ , respectively. These results show that adsorption of  $\text{N}_2$  is enhanced by the presence of intercalated  $\text{K}_4\text{H}$ , which is in line with our experimental finding that intercalation of potassium hydride is essential for  $\text{N}_2$  activation. On the other hand, the activation and dissociation of  $\text{H}_2$  on  $\text{K}_4\text{HC}_{96}$  and  $\text{K}_4\text{C}_{96}$  (the model of  $\text{K}_4\text{HC}_{96}$  following removal of lattice H) is exothermic and thus energetically favourable (Supplementary Fig. 26 and Supplementary Table 5). This clearly demonstrates that dihydrogen from the gas phase is able to diffuse to, and become activated at, the H vacancy sites of the  $\text{K}_4(\text{H})$  active centre and, thus, replenish H consumed at the catalytically active site, which is also supported by our  $\text{D}_2$ -TPR experiments discussed above (Supplementary Figs. 22 and 23).

Next, we studied potential mechanisms for ammonia synthesis in our model, which may follow either a dissociative or associative pathway<sup>29</sup>. The dissociative pathway starts with the cleavage of

$\text{N}_2$ , followed by hydrogenation reactions. In the model of  $\text{K}_4\text{HC}_{96}$ , the direct dissociation of  $\text{N}_2$  molecules requires an energy barrier of  $4.18 \text{ eV}$  (red line in Fig. 6), which indicates that the dissociative mechanism is unlikely to occur at the moderate temperatures employed in our study. This is consistent with our experimental finding that  $\text{N}_2$  can reversibly desorb from the catalyst before hydrogenation (Supplementary Fig. 19) and thus the direct dissociation of  $\text{N}_2$  is not observed. In contrast, following the associative mechanism, hydrogenation of adsorbed  $\text{N}_2$  molecules occurs initially and the bond between nitrogen atoms is completely broken only later—concomitantly during the formation of the first ammonia molecule. This pathway can be further grouped into two phases: (1) alternating hydrogenation of the two nitrogen atoms in turn, and (2) the distal mechanism during which the nitrogen atom that is relatively farther away from the catalyst surface is hydrogenated first<sup>5,30</sup>. The conversion of  $\text{N}_2$  to  $\text{NH}_3$  on  $\text{K}_4\text{HC}_{96}$  following an alternating associative mechanism is energetically the most favourable pathway (reaction energetics are indicated by the black line in Fig. 6; geometries of the corresponding reaction intermediates and transition states are shown in Supplementary Figs. 27 and 28). In this alternating associative pathway, following favourable adsorption of  $\text{N}_2$  the consecutive hydrogenation of adsorbed  $\text{N}_2$  by dissociated H occurs, presenting a maximum energy barrier of  $0.92 \text{ eV}$  at transition state 3 (TS3). Hydrogenation of the intermediate  $\text{H}_2\text{NNH}_2^*$  leads to the formation of surface-adsorbed  $\text{NH}_2^*$  and  $\text{NH}_3^*$  (completing the cleavage of the  $\text{N}\equiv\text{N}$  bond). Next, desorption of the first  $\text{NH}_3$  molecule is the largest uphill energy step with a calculated reaction energy of  $0.67 \text{ eV}$ . Hence activation of the adsorbed  $\text{N}_2$  molecules via associative hydrogenation and the desorption of

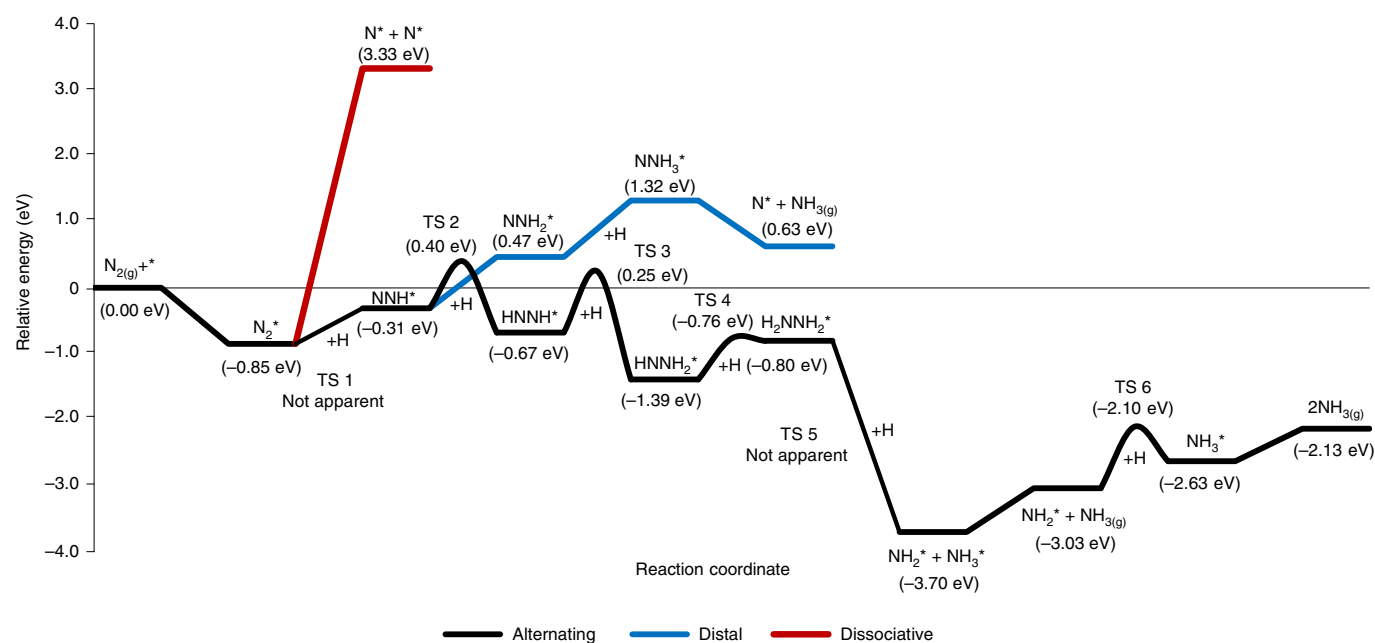


**Fig. 6 | DFT calculations for potential ammonia synthesis mechanisms on KH-intercalated graphite.** To represent the experimental study system, a  $K_4HC_{96}$  supercell model was employed in the DFT calculations of three different reaction mechanisms: alternating associative (black line) and distal associative (blue line) and dissociative (red line). The optimized geometries of all mechanism steps are presented in Supplementary Figs. 27 and 28. Note that transition states 1 (TS1) and 5 (TS5) are not real barriers because they have lower energies than either the product or reactant. TS1 and TS5 represent barriers to H migration between two neighbouring  $K_4$  sites.

generated ammonia represent potential kinetically slow steps in this reaction. The fact that the adsorption and subsequent dissociation of  $NH_3$  to  $^*NH_2$  is downhill (by 0.9 eV) and thus hinders the ammonia formation reaction is also in line with the observed negative reaction order for ammonia concentration in our experiments. Therefore, in support of our experimental results, DFT calculations suggest that the alternating associative mechanism is the most likely when employing the  $KH_{0.19}C_{24}$  catalyst for ammonia synthesis.

For the traditional Haber–Bosch process, ammonia synthesis is conducted at relatively high temperatures (400–500 °C) and pressures (10–30 MPa), conditions that provide sufficient thermal energy for direct cleavage of the  $N_2$  molecule, and thus the dissociation pathway is dominant. On the other hand, ammonia synthesis under milder conditions along this pathway may not be accessible. Therefore the associative pathway, bypassing the strong energy barrier of direct dinitrogen dissociation before hydrogenation, is highly interesting<sup>31,32</sup>. In this paper we demonstrate that, rather than using transition metals, KH species intercalated between graphene layers can facilitate stable adsorption of dinitrogen and cleavage of the  $N \equiv N$  bond following hydrogenation—in other words, an associative pathway. We believe that this finding can guide the search for materials development regarding low-temperature ammonia catalysts.

## Conclusions

In summary, we have developed an ammonia synthesis catalyst based on alkali metal hydride-intercalated graphite. The  $KH_{0.19}C_{24}$  catalyst was prepared by intercalation of KH into the layers of a graphite host material. The  $KH_{0.19}C_{24}$  catalyst shows stable  $NH_3$  productivity ( $\mu mol_{NH_3} g_{cat}^{-1} h^{-1}$ ) at temperatures of 250–400 °C, which is comparable to the 5 wt% Ru/MgO catalyst under identical reaction conditions. It appears that the presence of hydride facilitates the adsorption and activation of dinitrogen on the  $KH_{0.19}C_{24}$  catalyst, while subsequent hydrogenation can generate  $NH_3$  at

temperatures as low as 100 °C. Study of the mechanism involved shows that ammonia synthesis on potassium hydride-intercalated graphite follows an alternating associative pathway, which is distinct from the dissociative mechanism in traditional Ru or Fe catalysts. The present results will stimulate broad interest in the catalysis of ammonia synthesis by employing earth-abundant and inexpensive materials.

## Methods

**Materials.** All chemicals were stored in an Ar-filled glove box ( $O_2$   $\leq$  1 ppm,  $H_2O$   $\leq$  1 ppm). GNP500 (graphite nanoplatelets with a specific surface area of  $500 m^2 g^{-1}$ ), GNP750 (graphite nanoplatelets with a specific surface area of  $750 m^2 g^{-1}$ ), HSAG500 (high-surface-area graphite with a surface area of  $500 m^2 g^{-1}$ ), NPG (non-porous graphite) and carbon nanofibres were obtained from Imerys Graphite and Carbon. Carbon aerogel was prepared using the sol–gel resorcinol procedure reported previously<sup>33</sup>. All carbon supports were dried at 550 °C for 6 h under Ar flow before storage in a glovebox. Metallic K (98.0%), Ru(III) acetylacetonate (99.5%), magnesium oxide (99.5%), iron(III) acetylacetonate (99.9%) and nickel(II) acetylacetonate (95%) were purchased from Sigma-Aldrich.  $KNH_2$  powder was prepared by treating metallic potassium with liquid  $NH_3$  (0.8 MPa pressure) at room temperature for 1 week.

**Preparation of carbon-supported KH.** KH/carbon with a KH loading of 15 wt% was prepared by melt infiltration. Inside the argon-filled glove box, 57 mg of metallic K slices was mixed with 320 mg of carbon support. The mixture sample was placed in a graphite sample holder and inserted into a stainless steel autoclave. The autoclave was pressurized with  $H_2$  to 1 MPa, heated to 75 °C and held for 10 h. After cooling to room temperature, the remaining gas was vented. The sample was removed from the autoclave and stored in the glovebox.

**Preparation of the  $KH_{0.19}C_{24}$  catalyst.** The  $KH_{0.19}C_{24}$  catalyst was prepared by heating 200 mg of 15 wt% KH/carbon sample in an Ar flow at 400 °C for 2 h. The fresh catalyst was stored inside the glovebox.

**Catalytic reaction tests.** Ammonia synthesis activity was measured in a home-built, fixed-bed reactor. Catalysts were loaded in a quartz-lined tube (inner diameter, 8 mm; outer diameter, 11 mm) and placed inside the reactor. A continuous flow of gas ( $N_2:H_2$  1:3, purity  $>99.9999\%$ ) was supplied as reactant. Typically, 100 mg of catalyst was used and the reaction temperature was raised

at a ramp rate of 5 °C min<sup>-1</sup> under a given pressure (0.1–1.0 MPa) and flow rate (5–75 ml min<sup>-1</sup>). NH<sub>3</sub> in the outlet gas was trapped in a diluted sulfuric acid solution. The amount of NH<sub>3</sub><sup>+</sup> generated in the solution was analysed using a conductivity meter (Mettler Toledo SevenMulti), and thus catalytic performance was determined. A detailed product quantitative analysis is shown in Supplementary Fig. 3. The error range of ammonia synthesis performance on the KH<sub>0.19</sub>C<sub>24</sub> catalyst was within ±6%. We also conducted an experiment to demonstrate that the conductivity of the solution is stable, via a blank test over 36 h (Supplementary Fig. 4). In addition, we also use a Hidden mass spectrometer to double-check the production of ammonia (Supplementary Fig. 5). Gas products were analysed using the Hidden QIC mass analyser. This experiment was performed at the Dalian Institute of Chemical Physics, Chinese academy of Sciences. The results are consistent with those from the conductivity test.

**Kinetic measurements.** The measurements for determination of apparent activation energy and reaction orders of N<sub>2</sub>, H<sub>2</sub> and NH<sub>3</sub> followed methods reported previously<sup>11,14</sup>. For all kinetic measurements, conversion levels were kept <2% to make sure that measurement conditions were far from thermodynamic equilibrium (at 1 MPa and 400 °C, thermodynamic equilibrium conversion was 7.1%). All measurements were conducted under a total pressure of 1 MPa and at 400 °C. Measurements for the reaction orders in N<sub>2</sub> or H<sub>2</sub> were conducted in a flow of mixed gas (N<sub>2</sub>/H<sub>2</sub>/Ar). The reaction order in N<sub>2</sub> was measured at a constant H<sub>2</sub> pressure of 0.5 MPa while changing the partial pressures of N<sub>2</sub> and Ar. The gas percentage compositions of N<sub>2</sub>/H<sub>2</sub>/Ar were 10/50/40, 20/50/30, 30/50/20 and 40/50/10. The reaction order in H<sub>2</sub> was measured at a constant N<sub>2</sub> pressure of 0.15 MPa while changing the partial pressures of H<sub>2</sub> and Ar. The percentage gas compositions of N<sub>2</sub>/H<sub>2</sub>/Ar were 15/30/55, 15/40/45, 15/50/35 and 15/60/25. The reaction order in NH<sub>3</sub> was determined with a flow of gas (N<sub>2</sub>:H<sub>2</sub>:1:3) by changing the synthesis gas flow rates (100 mg of catalyst, 5–75 ml min<sup>-1</sup>, space velocity (SV) = 3,000–45,000 ml g<sub>cat</sub><sup>-1</sup> h<sup>-1</sup>)<sup>28</sup>.

**N<sub>2</sub> treatment.** The fresh KH<sub>0.19</sub>C<sub>24</sub> catalyst was loaded and placed in a graphite sample holder and inserted into a stainless steel autoclave. An initial pressure of 0.5 MPa N<sub>2</sub> was applied, and the sample was heated to 300 °C for 20 h. After cooling, this N<sub>2</sub>-treated sample was removed from the autoclave and stored in the Ar glovebox.

**Hydrogenation of N<sub>2</sub>-treated KH<sub>0.19</sub>C<sub>24</sub>.** Hydrogenation of the N<sub>2</sub>-treated KH<sub>0.19</sub>C<sub>24</sub> catalyst was performed in a Micromeritics AutoChem II set-up coupled with a Hidden mass spectroscopy. Typically, 30 mg of catalyst was loaded in a quartz reactor and the temperature raised to 400 °C (ramp rate of 5 °C min<sup>-1</sup>) in a flow of 5% H<sub>2</sub>/Ar at ambient pressure. The outlet gas (NH<sub>3</sub>) was analysed using the Hidden QIC mass analyser.

**Isotopic tests.** Isotopic tests were performed using a gas flow of 75% D<sub>2</sub>/25% Ar at ambient pressure in a Micromeritics AutoChem II set-up coupled with a Hidden mass spectroscopy. Gas products were analysed using the Hidden QIC mass analyser.

**Characterization.** X-ray diffraction patterns were conducted from 2θ = 20–80° with a Bruker AXS D8 Advance XRD instrument using CoK<sub>α</sub> radiation with a wavelength of 1.79026 Å. An airtight sample holder was used to prevent ingress of air. N<sub>2</sub> physisorption measurements were performed at –196 °C using the Micromeritics Tristar 3000 apparatus. Micropore volume was calculated using the *t*-plot method. Barrett–Joyner–Halenda pore size distribution and mesopore volume were determined from the adsorption branch of isotherms. ICP analysis was carried out using an ICP-OES Perkin-Elmer Analyst 200 spectrometer combined with a C/N/S analyser. Measurements were conducted at MIKROLAB. Before commencing measurements, each sample was digested using reverse aqua regia in a Mars-6 digestion microwave system (CEM Corp.). Typically, 20 mg of sample was weighed into the commercial vessel followed by the addition of a 10-ml mixture of 3:1 HNO<sub>3</sub>:HCl. The sample was digested at 210 °C for 45 min. Following digestion, the sample was diluted to 25 ml with deionized water for measurement. Quantitative analyses were established by measuring Perkin-Elmer multi-element standard solutions. All detections are based on a 98% confidence level (three standard deviations). HAADF-STEM and EDX images were obtained using a Tecnai 20FEG (Thermo Fisher Scientific, formerly known as FEI) microscope with a field emission gun operated at 200 kV. The electron diffraction pattern was determined using a camera constant of 720. The sample was deposited onto the copper grid inside the Ar-filled glovebox and transferred to the electron microscope in an airtight sample holder. XPS was performed on a Thermo Scientific K-alpha spectrometer equipped with a monochromatic small-spot X-ray source and a 180° double-focusing hemispherical analyser with a 128-channel delay line detector. Spectra were obtained using an aluminium anode (hν(Al K<sub>α</sub>) = 1,486.6 eV) operated at 72 W and a spot size of 400 μm. Samples were mounted on a vacuum/inert gas sample holder by conductive carbon tape and transported and handled under inert conditions (Ar glovebox). Sample charging was compensated for by the use of an electron flood gun. Binding energy was calibrated to the C 1s peak of either graphitic sp<sup>2</sup> carbon (284.5 eV) or adventitious carbon (284.8 eV).

**Theoretical calculations.** All DFT calculations reported in this work were performed using the Vienna ab initio Simulation Package v.5.4.1 (refs. <sup>34–36</sup>). The projector augmented wave method was employed to describe electron–ion interactions. A kinetic energy cut-off of 500 eV was used for the planewave basis<sup>37,38</sup>. We used the Perdew–Burke–Ernzerhof exchange–correlation functional of the generalized gradient approximation<sup>39</sup>. The convergence criteria for structural optimizations were that the total forces acting on each atom must be <0.015 eV Å<sup>-1</sup>. The global break condition for the electronic self-consistent loop was set to 10<sup>-6</sup> eV. To take into account van der Waals interactions, the zero-damping DFT–D3 method was employed<sup>40</sup>. The effects of spin polarization were considered during both bulk and slab calculations. After initial tests, data from non-spin-polarized calculations was used. The four-atom-containing hexagonal P6<sub>3</sub>/mmc graphite crystal lattice was adopted from Materials Project (mp-48)<sup>41</sup>. Optimization of graphite was completed using an automatically generated 33 × 33 × 33 Monkhorst–Pack *k*-point mesh and a sequence of consecutive volume and ionic relaxation calculations, until the total energy difference between the two final consecutive ionic steps was <1 meV<sup>42</sup>.

Establishment of computational models is based on the experimental results. The hydrogen content quantification result shows that ~24% hydrogen remained in the catalyst after the intercalation process, which provides a molar ratio of 4:1 for K:H in the catalyst. In addition, ICP elemental analysis shows that the stoichiometry of K:C in the catalyst is 1:24. Therefore, a K<sub>4</sub>HC<sub>96</sub> slab model with 101 atoms was used for the calculation of ammonia synthesis. The four-layer graphite slab with 96 C atoms was prepared using the 4 × 3 × 2 supercell of the optimized graphite crystal. To avoid interactions between the periodic images of the slabs, a vacuum spacing of 15 Å was added to both sides of the graphite slab, totalling 30 Å between the periodic images, in the direction perpendicular to the graphite layers. After performing a *k*-point test on the graphite slab model in all slab calculations, an automatically generated 4 × 4 × 1 Monkhorst–Pack *k*-point mesh was used, which deviated from the denser *k*-point sets by >0.5 meV per Catom<sup>42</sup>. Multiple structures were studied as initial candidates for the structural model (K<sub>4</sub>HC<sub>96</sub>) of the potassium hydride-intercalated graphite at stage 2. Computational results show that the planar orientation at which the intercalated K<sub>4</sub>H unit was placed—in the middle layer of the four-layer graphite slab (C<sub>96</sub>)—was the most stable structure and was thus used for study of the reaction mechanism (Supplementary Fig. 25). Charge distributions among atoms of the chemical compounds were obtained from Bader charge analysis<sup>43</sup>. A fine fast Fourier transform grid, required to reproduce total core charge accurately, was employed by setting all NG(X,Y,Z)F values at 400. Ammonia synthesis mechanisms were studied on the optimized K<sub>4</sub>HC<sub>96</sub> geometry by keeping the bottom two graphite layer carbon atoms fixed in their optimized positions. For all intermediate steps, several initial estimates for the positions of H and N atoms and N<sub>2</sub>H<sub>2</sub> intermediate species were considered, and those optimized configurations with the lowest total energies are shown in Supplementary Fig. 27. Energies of H<sub>2</sub>, N<sub>2</sub> and NH<sub>3</sub> molecules were computed in 15-Å cubic cells. All visual representations of the computed geometries were prepared using Vesta v.3.5.3 (refs. <sup>43</sup>). Equations (1) and (2) were used to compute the intercalation energy (ΔE<sup>int</sup>) and reaction energies (ΔE<sup>Rxn</sup>):

$$\Delta E^{\text{int}} = E_{\text{C}_{96}\text{K}_4\text{H}} - (E_{\text{C}_{96}} + 4 E_{\text{K}_{\text{Bulk}}} + 1/2 E_{\text{H}_2}) \quad (1)$$

$$\Delta E^{\text{Rxn}} = \sum E_{\text{Products}} - \sum E_{\text{Reactants}} \quad (2)$$

$E_{\text{C}_{96}\text{K}_4\text{H}}$ ,  $E_{\text{C}_{96}}$ ,  $E_{\text{K}_{\text{Bulk}}}$  and  $E_{\text{H}_2}$  represent the total energies of the potassium hydride-intercalated graphite, graphite, bulk potassium and hydrogen molecules, respectively.  $\sum E_{\text{Products}}$  and  $\sum E_{\text{Reactants}}$  are different for each reaction step. For example, for N<sub>2</sub> adsorption ( $\Delta E^{\text{Ads}}(\text{N}_2)$ ),  $\sum E_{\text{Products}}$  is the total energy of the system after N<sub>2</sub> binding and  $\sum E_{\text{Reactants}}$  is the sum of the total energies of K<sub>4</sub>HC<sub>96</sub> and the N<sub>2</sub> molecule in the gas phase.

Distances of two adjacent graphene layers sandwiching K<sub>4</sub>H in the alternating associative pathway are shown in Supplementary Table 6.

The climbing image-nudged elastic band (NEB) procedure was used for the determination of transition state geometries<sup>44</sup>. The positions of H atoms were obtained from the calculations for the H<sub>2</sub> dissociation reaction, and these H positions were then used as initial configurations in NEB calculations. All NEB calculations were performed with at least six intermediate geometries.

## Data availability

The data supporting the findings of this study are available within the article and the Supplementary Information. Atomic coordinates of the optimized computational models are supplied as Supplementary Data 1. All raw data are available on reasonable request by contacting the corresponding authors. Source data are provided with this paper.

Received: 12 January 2020; Accepted: 8 February 2022;  
Published online: 17 March 2022



## References

- Guo, J. P. & Chen, P. NH<sub>3</sub> as an energy carrier. *Chem* **3**, 709–712 (2017).
- Erisman, J. W., Sutton, M. A., Galloway, J., Klimont, Z. & Winiwarter, W. How a century of ammonia synthesis changed the world. *Nat. Geosci.* **1**, 636–639 (2008).
- Schlogl, R. Catalytic synthesis of ammonia a “never-ending story”? *Angew. Chem. Int. Ed. Engl.* **42**, 2004–2008 (2003).
- Zeng, H. S., Inazu, K. & Aika, K. The working state of the barium promoter in ammonia synthesis over an active-carbon-supported ruthenium catalyst using barium nitrate as the promoter precursor. *J. Catal.* **211**, 33–41 (2002).
- Foster, S. L. et al. Catalysts for nitrogen reduction to ammonia. *Nat. Catal.* **1**, 490–500 (2018).
- Chen, J. G. et al. Beyond fossil fuel-driven nitrogen transformations. *Science* **360**, aar6611 (2018).
- Kitano, M. et al. Electride support boosts nitrogen dissociation over ruthenium catalyst and shifts the bottleneck in ammonia synthesis. *Nat. Commun.* **6**, 6731 (2015).
- Medford, A. J. et al. From the Sabatier principle to a predictive theory of transition-metal heterogeneous catalysis. *J. Catal.* **328**, 36–42 (2015).
- Makepeace, J. W. et al. Reversible ammonia-based and liquid organic hydrogen carriers for high-density hydrogen storage: recent progress. *Int. J. Hydrog. Energy* **44**, 7746–7767 (2019).
- Kitano, M. et al. Self-organized ruthenium-barium core-shell nanoparticles on a mesoporous calcium amide matrix for efficient low-temperature ammonia synthesis. *Angew. Chem. Int. Ed. Engl.* **57**, 2648–2652 (2018).
- Kitano, M. et al. Ammonia synthesis using a stable electride as an electron donor and reversible hydrogen store. *Nat. Chem.* **4**, 934–940 (2012).
- Ogura, Y. et al. Efficient ammonia synthesis over a Ru/La<sub>0.5</sub>Ce<sub>0.5</sub>O<sub>1.75</sub> catalyst pre-reduced at high temperature. *Chem. Sci.* **9**, 2230–2237 (2018).
- Manabe, R. et al. Electrocatalytic synthesis of ammonia by surface proton hopping. *Chem. Sci.* **8**, 5434–5439 (2017).
- Wang, P. K. et al. Breaking scaling relations to achieve low-temperature ammonia synthesis through LiH-mediated nitrogen transfer and hydrogenation. *Nat. Chem.* **9**, 64–71 (2017).
- Chang, F. et al. Alkali and alkaline earth hydrides-driven N<sub>2</sub> activation and transformation over Mn nitride catalyst. *J. Am. Chem. Soc.* **140**, 14799–14806 (2018).
- Wang, P. K. et al. The formation of surface lithium-iron ternary hydride and its function on catalytic ammonia synthesis at low temperatures. *Angew. Chem. Int. Ed. Engl.* **56**, 8716–8720 (2017).
- Kobayashi, Y. et al. Titanium-based hydrides as heterogeneous catalysts for ammonia synthesis. *J. Am. Chem. Soc.* **139**, 18240–18246 (2017).
- Tang, Y. et al. Metal-dependent support effects of oxyhydride-supported Ru, Fe, Co catalysts for ammonia synthesis. *Adv. Energy Mater.* **8**, 1801772 (2018).
- Azofra, L. M. et al. Single-site molybdenum on solid support materials for catalytic hydrogenation of N<sub>2</sub> into NH<sub>3</sub>. *Angew. Chem. Int. Ed. Engl.* **57**, 15812–15816 (2018).
- Bramwell, P. L. et al. A transition-metal-free hydrogenation catalyst: pore-confined sodium alanate for the hydrogenation of alkynes and alkenes. *J. Catal.* **344**, 129–135 (2016).
- Enoki, T., Miyajima, S., Sano, M. & Inokuchi, H. Hydrogen alkali-metal graphite ternary intercalation compounds. *J. Mater. Res.* **5**, 435–466 (1990).
- Morawski, A. W. Application of CoCl<sub>2</sub>-K graphite-intercalation compounds in catalysis. *Synth. Met.* **59**, 249–252 (1993).
- Salamanca-Riba, L., Yeh, N. C., Dresselhaus, M. S., Endo, M. & Enoki, T. High-resolution transmission electron microscopy on KH<sub>x</sub>-GICs. *J. Mater. Res.* **1**, 177–186 (1986).
- Ertl, G. & Thiele, N. XPS studies with ammonia synthesis catalysts. *Appl. Surf. Sci.* **3**, 99–112 (1979).
- Gaol, W. B. et al. Production of ammonia via a chemical looping process based on metal imides as nitrogen carriers. *Nat. Energy* **3**, 1067–1075 (2018).
- Rosowski, F. et al. Ruthenium catalysts for ammonia synthesis at high pressures: preparation, characterization, and power-law kinetics. *Appl. Catal. A* **151**, 443–460 (1997).
- Urabe, K., Aika, K. & Ozaki, A. Activation of nitrogen by alkali metal-promoted transition-metal. 6. Hydrogen effect on isotopic equilibration of nitrogen and rate-determining step of ammonia-synthesis on potassium-promoted ruthenium catalysts. *J. Catal.* **42**, 197–204 (1976).
- Hagen, S. et al. Ammonia synthesis with barium-promoted iron-cobalt alloys supported on carbon. *J. Catal.* **214**, 327–335 (2003).
- Suryanto, B. H. R. et al. Challenges and prospects in the catalysis of electroreduction of nitrogen to ammonia. *Nat. Catal.* **2**, 290–296 (2019).
- Yan, X. et al. Nitrogen reduction to ammonia on atomic-scale active sites under mild conditions. *Small Methods* **3**, 1800501 (2019).
- Zheng, J. et al. Efficient non-dissociative activation of dinitrogen to ammonia over lithium-promoted ruthenium nanoparticles at low pressure. *Angew. Chem. Int. Ed. Engl.* **58**, 17335–17341 (2019).
- Wang, X. Y. et al. Insight into dynamic and steady-state active sites for nitrogen activation to ammonia by cobalt-based catalyst. *Nat. Commun.* **11**, 653 (2020).
- Pekala, R. W. Organic aerogels from the polycondensation of resorcinol with formaldehyde. *J. Mater. Sci.* **24**, 3221–3227 (1989).
- Kresse, G. & Hafner, J. Ab initio molecular dynamics for open-shell transition metals. *Phys. Rev. B* **48**, 13115–13118 (1993).
- Kresse, G. & Furthmüller, J. Efficient iterative schemes for ab initio total-energy calculations using a plane-wave basis set. *Phys. Rev. B* **54**, 11169–11186 (1996).
- Kresse, G. & Furthmüller, J. Efficiency of ab-initio total energy calculations for metals and semiconductors using a plane-wave basis set. *Comput. Mater. Sci.* **6**, 15–50 (1996).
- Blöchl, P. E. Projector augmented-wave method. *Phys. Rev. B* **50**, 17953–17979 (1994).
- Kresse, G. & Joubert, D. From ultrasoft pseudopotentials to the projector augmented-wave method. *Phys. Rev. B* **59**, 1758–1775 (1999).
- Perdew, J. P., Burke, K. & Ernzerhof, M. Generalized gradient approximation made simple. *Phys. Rev. Lett.* **77**, 3865–3868 (1996).
- Grimme, S., Antony, J., Ehrlich, S. & Krieg, H. A consistent and accurate ab initio parametrization of density functional dispersion correction (DFT-D) for the 94 elements H-Pu. *J. Chem. Phys.* **132**, 154104 (2010).
- Persson, K. LBNL Materials Project. <https://materialsproject.org> (2014).
- Monkhorst, H. J. & Pack, J. D. Special points for Brillouin-zone integrations. *Phys. Rev. B* **13**, 5188–5192 (1976).
- Tang, W., Sanville, E. & Henkelman, G. A grid-based Bader analysis algorithm without lattice bias. *J. Phys. Condens. Matter* **21**, 084204 (2009).
- Henkelman, G., Uberuaga, B. P. & Jonsson, H. A climbing image nudged elastic band method for finding saddle points and minimum energy paths. *J. Chem. Phys.* **113**, 9901–9904 (2000).

## Acknowledgements

We thank S. Zanoni for N<sub>2</sub> physisorption measurements, and Netherlands Organisation for Scientific Research (NWO)-Vici (no. 16.130.344) for overall funding of the project. P.N. and P.E.d.J. acknowledge support from the European Research Council under the European Union's Horizon 2020 research and innovation programme (ERC-2014-CoG, no. 648991). S.E. acknowledges funding from the initiative 'Computational Sciences for Energy Research' from Shell and NWO grant no. 15CSTT05. The computational part of this work was sponsored by NWO Exact and Natural Sciences for the use of supercomputer facilities. We thank P. Chen and J. Guo for useful discussions.

## Author contributions

P.E.d.J. and P.N. conceived and supervised the research. F.C. designed and performed experiments and data analysis. I.T. and S.E. performed DFT calculations and results analysis. J.W.d.R. constructed the set-up for catalytic activity tests. J.P.H. performed XPS analysis. J.D.M. was responsible for electron microscopy measurements. F.C., P.N. and P.E.d.J. wrote the paper, with I.T. and S.E. contributing the section on DFT calculations. All authors commented on the manuscript.

## Competing interests

The authors declare no competing interests.

## Additional information

**Supplementary information** The online version contains supplementary material available at <https://doi.org/10.1038/s41929-022-00754-x>.

**Correspondence and requests for materials** should be addressed to Peter Ngene or Petra E. de Jongh.

**Peer review information** *Nature Catalysis* thanks the anonymous reviewers for their contribution to the peer review of this work.

**Reprints and permissions information** is available at [www.nature.com/reprints](http://www.nature.com/reprints).

**Publisher's note** Springer Nature remains neutral with regard to jurisdictional claims in published maps and institutional affiliations.

© The Author(s), under exclusive licence to Springer Nature Limited 2022